Spatial, Temporal, and Spectral Aspects of Far-Field Radar Data

Margaret Cheney[1] and Ling Wang[2]
[1]Departments of Mathematical Sciences
[2]Department of Electrical, Computer, and Systems Engineering
Rensselaer Polytechnic Institute
Troy, NY 12180

Brett Borden
Physics Department
Naval Postgraduate School
Monterey, CA 93943-5001

***Abstract*— We develop a linearized imaging theory that combines the spatial, temporal, and spectral aspects of scattered waves. We consider the case of fixed, distributed transmitters and receivers, and a general distribution of objects, each undergoing linear motion; thus the theory deals with imaging distributions in phase space. We derive a model for the data that is appropriate for any waveform, and show how it specializes to familiar results when the targets are far from the antennas and narrowband waveforms are used.**

We use a phase-space imaging formula that can be interpreted in terms of filtered backprojection or matched filtering. For this imaging approach, we derive the corresponding point-spread function. We plot examples of this point-spread function for three different geometrical placements of the transmitters and receivers.

Special cases of the theory reduce to: a) Range-Doppler imaging, b) Inverse Synthetic Aperture Radar (ISAR) and Spotlight Synthetic Aperture Radar (SAR), c) Diffraction Tomography or Ultra-Narrowband Tomography, and d) Tomography of Moving Targets.

I. Introduction

It is well-known [4], [8] that radar systems can measure both range and velocity of a target, and the resolution in range and velocity depends, via the radar ambiguity function, on the waveform used. Ambiguity-function-based range-Doppler imaging appears at the bottom plane in Fig. 1. Most SAR imaging systems, on the other hand, use a sequence of high-range-resolution pulses, transmitted from a diversity of spatial positions, to form an image of stationary targets. SAR and ISAR, which are closely related, appear on the back plane of Fig. 1. It is also possible to use a sequence of high-Doppler-resolution pulses, transmitted from a diversity of spatial positions, to form an image [2] of stationary targets. Such Doppler SAR techniques appear on the left side of Fig. 1. This diagram suggests the question "What is in the middle of the diagram? How can we combine the spatial, temporal, and spectral aspects of radar data?"

Below we develop a theory that shows how to unify these different imaging approaches. In the process, we will demonstrate how we can fuze the spatial, temporal, and spectral aspects of scattered-field-based imaging. For simplicity, we consider only the far-field case, the general case being published elsewhere [3]. The present discussion deals with the case of fixed distributed sensors, although our results include monostatic configurations (in which a single transmitter and receiver are co-located) as a special case. Methods for imaging stationary scenes in the case when the transmitters and receivers are located at different positions have been particularly well-developed in the geophysics literature [1] and have also been explored in the radar literature [10], [11], [12]. In this paper we consider scenes containing multiple moving objects.

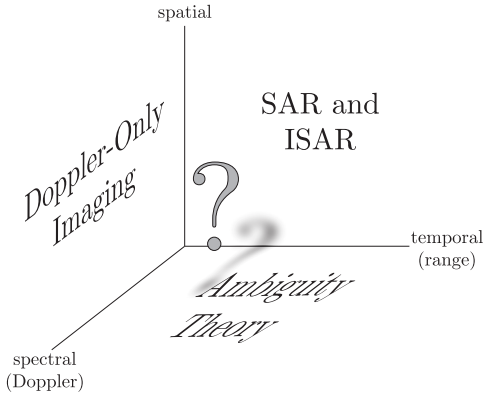

Fig. 1. A diagram of various theories that combine spatial, spectral, and temporal aspects of scattered waves.

II. Model for Data

We model wave propagation and scattering by the scalar wave equation for the wavefield $\psi(t,\boldsymbol{x})$ due to a source waveform $s(t,\boldsymbol{x})$ transmitted from location $\boldsymbol{y}$:

$$[\nabla^2 - c^{-2}(t,\boldsymbol{x})\partial_t^2]\psi(t,\boldsymbol{x},\boldsymbol{y}) = \delta(\boldsymbol{x}-\boldsymbol{y})s_{\boldsymbol{y}}(t)\,. \qquad (1)$$

For simplicity, we consider only localized isotropic sources; the work can easily be extended to more realistic antenna models [9].

A single scatterer moving at velocity $\boldsymbol{v}$ corresponds to an index-of-refraction distribution $n^2(\boldsymbol{x}-\boldsymbol{v}t)$:

$$c^{-2}(t,\boldsymbol{x}) = c_0^{-2}[1+n^2(\boldsymbol{x}-\boldsymbol{v}t)]\,, \qquad (2)$$

where c_0 denotes the speed in the stationary background medium (here assumed constant). For radar, c_0 is the speed of light in vacuum. We write $q_{\boldsymbol{v}}(\boldsymbol{x}-\boldsymbol{v}t) = c_0^{-2}n^2(\boldsymbol{x}-\boldsymbol{v}t)$. To model multiple moving scatterers, we let $q_{\boldsymbol{v}}(\boldsymbol{x}-\boldsymbol{v}t)\,d^3x\,d^3v$

be the corresponding quantity for the scatterers in the volume $d^3x\,d^3v$ centered at $(\boldsymbol{x},\boldsymbol{v})$. In other words, q is a distribution in *phase space*, and $q_{\boldsymbol{v}}$ is the spatial distribution, at time $t=0$, of scatterers moving with velocity $\boldsymbol{v}$. Consequently, the scatterers in the spatial volume d^3x (at $\boldsymbol{x}$) give rise to

$$c^{-2}(t,\boldsymbol{x}) = c_0^{-2} + \int q_{\boldsymbol{v}}(\boldsymbol{x}-\boldsymbol{v}t)\,d^3v\,. \tag{3}$$

We note that the physical interpretation of $q_{\boldsymbol{v}}$ involves a choice of a time origin. A choice that is particularly appropriate, in view of our assumption about linear target velocities, is a time during which the wave is interacting with targets of interest. The wave equation corresponding to (3) is then

$$\left[\nabla^2 - c_0^{-2}\partial_t^2 - \int q_{\boldsymbol{v}}(\boldsymbol{x}-\boldsymbol{v}t)\,d^3v\,\partial_t^2\right]\psi(t,\boldsymbol{x}) = s_{\boldsymbol{y}}(t)\delta(\boldsymbol{x}-\boldsymbol{y})\,. \tag{4}$$

With the Born (single-scattering) approximation and far-field approximation, the scattered field can be written [3]

$$\psi_{\rm f}^{\rm sc}(t,\boldsymbol{z},\boldsymbol{y}) = \int \frac{\ddot{s}_{\boldsymbol{y}}\left[\phi(\boldsymbol{x},\boldsymbol{v})\right]}{(4\pi)^2|\boldsymbol{z}||\boldsymbol{y}|} q_{\boldsymbol{v}}(\boldsymbol{x})\,d^3x\,d^3v \tag{5}$$

where

$$\phi(\boldsymbol{x},\boldsymbol{v}) = \alpha_{\boldsymbol{v}}\left(t - |\boldsymbol{z}|/c + \hat{\boldsymbol{z}}\cdot\boldsymbol{x}/c\right) - |\boldsymbol{y}|/c + \hat{\boldsymbol{y}}\cdot\boldsymbol{x}/c \tag{6}$$

and where α denotes the Doppler scale factor

$$\alpha_{\boldsymbol{v}} = \frac{1+\widehat{\boldsymbol{y}}\cdot\boldsymbol{v}/c}{1-\widehat{\boldsymbol{z}}\cdot\boldsymbol{v}/c}. \tag{7}$$

In the case when $|\boldsymbol{v}|/c \ll 1$, we have $\alpha_{\boldsymbol{v}} \approx 1 + (\hat{\boldsymbol{y}}+\hat{\boldsymbol{z}})\cdot\boldsymbol{v}/c$.

To write (5) as a Fourier Integral Operator, we write $s_{\boldsymbol{y}}(t)$ in terms of its inverse Fourier transform:

$$s_{\boldsymbol{y}}(t) = \frac{1}{2\pi}\int e^{-i\omega' t} S_{\boldsymbol{y}}(\omega)\,d\omega'\,. \tag{8}$$

With (8), we convert (5) into

$$\psi_{\rm f}^{\rm sc}(t,\boldsymbol{z},\boldsymbol{y}) = \int \frac{(-i\omega)^2 S_{\boldsymbol{y}}(\omega)}{(4\pi)^2|\boldsymbol{z}||\boldsymbol{y}|} e^{-i\omega\phi(\boldsymbol{x},\boldsymbol{v})}\,d\omega q_{\boldsymbol{v}}(\boldsymbol{x})\,d^3x\,d^3v. \tag{9}$$

III. Image Formation

The corresponding imaging operation is a filtered version of the formal adjoint of the "forward" operator given by (9). Thus we form the phase-space image $I(\boldsymbol{p},\boldsymbol{u})$ of $q_{\boldsymbol{u}}(\boldsymbol{p})$ as

$$I(\boldsymbol{p},\boldsymbol{u}) = \sum_{\boldsymbol{y},\boldsymbol{z}}\int e^{i\omega[\phi(\boldsymbol{p},\boldsymbol{u})]} Q_\infty(\omega,\boldsymbol{p},\boldsymbol{u},\boldsymbol{z},\boldsymbol{y})\,d\omega \times\psi^{\rm sc}(t,\boldsymbol{z},\boldsymbol{y})\,dt. \tag{10}$$

Here $\boldsymbol{p}$ represents the position coordinate and $\boldsymbol{u}$ the velocity.

The specific choice of filter is dictated by various considerations [1], [13]; here we choose Q so that the resulting formulas are connected with familiar theories. We take the filter to be

$$Q(\omega,\boldsymbol{p},\boldsymbol{u},\boldsymbol{z},\boldsymbol{y}) = -\frac{(4\pi)^2|\boldsymbol{z}||\boldsymbol{y}|S_{\boldsymbol{y}}^*(\omega)J(\omega,\boldsymbol{p},\boldsymbol{u},\boldsymbol{z},\boldsymbol{y})\alpha_{\boldsymbol{u}}}{\omega^2}\,, \tag{11}$$

which leads (below) to the matched filter. Here the star denotes complex conjugation, and J is a geometrical factor [3] that depends on the configuration of transmitters and receivers.

IV. Analysis of the Point-Spread Function

We obtain the point-spread function of the imaging system by substituting (9) into (10). We thus obtain an image of the form

$$I(\boldsymbol{p},\boldsymbol{u}) = \int K(\boldsymbol{p},\boldsymbol{u};\boldsymbol{x},\boldsymbol{v}) q_{\boldsymbol{v}}(\boldsymbol{x}) d^3x d^3v, \tag{12}$$

where an approximation to the point-spread function K is given below.

Many radar systems use a narrowband waveform, which is of the form

$$s_{\boldsymbol{y}}(t) = \tilde{s}_{\boldsymbol{y}}(t)\,e^{-i\omega_{\boldsymbol{y}}t} \tag{13}$$

where $\tilde{s}(t,\boldsymbol{y})$ is slowly varying, as a function of t, in comparison with $\exp(-i\omega_{\boldsymbol{y}}t)$, where $\omega_{\boldsymbol{y}}$ is the carrier frequency for the transmitter at position $\boldsymbol{y}$. For the narrowband case, we write $K^{(\rm NB)}$ instead of K.

In the narrowband case, the point-spread function reduces to [3]

$$\boxed{K^{(\rm NB)}(\boldsymbol{p},\boldsymbol{u};\boldsymbol{x},\boldsymbol{v}) = \sum_{\boldsymbol{y},\boldsymbol{z}} \omega_{\boldsymbol{y}}^2 e^{i\Phi_{\boldsymbol{y},\boldsymbol{z}}}\tilde{J}(\boldsymbol{p},\boldsymbol{u},\boldsymbol{z},\boldsymbol{y}) \times A_{\boldsymbol{y}}\Big(k_{\boldsymbol{y}}(\hat{\boldsymbol{y}}+\hat{\boldsymbol{z}})\cdot(\boldsymbol{u}-\boldsymbol{v}),\ (\hat{\boldsymbol{z}}+\hat{\boldsymbol{y}})\cdot(\boldsymbol{x}-\boldsymbol{p})/c\Big)\,,} \tag{14}$$

where $\tilde{J}$ is a geometrical factor closely related to J above, where

$$A_{\boldsymbol{y}}(\tilde{\omega},\tau) = e^{-i\omega_{\boldsymbol{y}}\tau}\int \tilde{s}_{\boldsymbol{y}}^*(t-\tau)\,\tilde{s}_{\boldsymbol{y}}(t)\,e^{i\tilde{\omega}t}\,dt\,. \tag{15}$$

is the narrowband ambiguity function (which is defined here to include a phase) and where

$$\Phi_{\boldsymbol{y},\boldsymbol{z}}(\boldsymbol{x},\boldsymbol{v},\boldsymbol{p},\boldsymbol{u}) = \tilde{\varphi}_{\boldsymbol{x},\boldsymbol{v}} - \tilde{\varphi}_{\boldsymbol{p},\boldsymbol{u}} - ik_{\boldsymbol{y}}(\beta_{\boldsymbol{u}}-\beta_{\boldsymbol{v}})(\hat{\boldsymbol{z}}+\hat{\boldsymbol{y}})\cdot\boldsymbol{x} \tag{16}$$

with $k_{\boldsymbol{y}} = \omega_{\boldsymbol{y}}/c$, $\beta_{\boldsymbol{v}} = (\hat{\boldsymbol{y}}+\hat{\boldsymbol{z}})\cdot\boldsymbol{v}/c$, and

$$\begin{aligned}\tilde{\varphi}_{\boldsymbol{x},\boldsymbol{v}} - \tilde{\varphi}_{\boldsymbol{p},\boldsymbol{u}} &= \frac{\omega_{\boldsymbol{y}}}{c}\left[[(1+\beta_{\boldsymbol{u}})\hat{\boldsymbol{z}}+\hat{\boldsymbol{y}}]\cdot\boldsymbol{p} - [(1+\beta_{\boldsymbol{v}})\hat{\boldsymbol{z}}+\hat{\boldsymbol{y}}]\cdot\boldsymbol{x}\right]\\ &= k_{\boldsymbol{y}}\left[(\hat{\boldsymbol{z}}+\hat{\boldsymbol{y}})\cdot(\boldsymbol{p}-\boldsymbol{x}) + \hat{\boldsymbol{z}}\cdot(\beta_{\boldsymbol{u}}\boldsymbol{p} - \beta_{\boldsymbol{v}}\boldsymbol{x})\right]\end{aligned} \tag{17}$$

The narrowband result (14) clearly exhibits the importance of the bistatic bisector vector $\hat{\boldsymbol{y}}+\hat{\boldsymbol{z}}$.

V. Examples of the Point-Spread Function

The point-spread function contains all the information about the performance of the imaging system. Unfortunately the PSF is difficult to visualize because it depends on so many variables: even in the case when the positions and velocities are restricted to a known plane, the PSF is a function of four variables.

We would like to know whether we can find both the position and velocity of moving targets. Ideally, the point-spread function is delta-like, and so we can obtain both position and velocity. If, however, the PSF is ridge-like, then there will be uncertainty in some directions or in some combination of positions and velocities.

In order to look for possible ridge-like behavior, we write the PSF as

$$K(\boldsymbol{p}, \boldsymbol{u}; \boldsymbol{x}, \boldsymbol{v}) = K(r(\cos\theta, \sin\theta), s(\cos\phi, \sin\phi), \boldsymbol{x}, \boldsymbol{v}). \tag{18}$$

We plot the PSF for a fixed target position $\boldsymbol{x}$ and target velocity $\boldsymbol{v}$. We then sample θ and ϕ at intervals of $\pi/4$, and for each choice of θ and ϕ, we plot r versus s. This process results in $9 \times 9 = 81$ plots of r versus s. Finally, to show the entire four-dimensional space at a glance, we display all the 81 plots simultaneously on a grid, arranged as shown in Fig. 2.

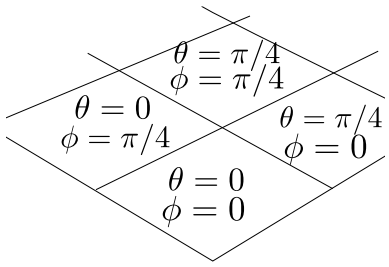

Fig. 2. This shows how Figures 3 - 5 display the four-dimensional point-spread function (18).

A. Simulation Parameters

Our strategy in the simulations is to use a delta-like ambiguity function, and investigate the effect of geometry on the overall point-spread function. In all cases, we use a transmit time of $T_{\boldsymbol{y}} = 0$.

1) Waveform: In the simulations, we use a high-Doppler-resolution, linearly-frequency-modulated (LFM) pulse train. The ambiguity function of this pulse train has a "bed-of-nails" appearance [8], with a delta-like central peak that has good velocity resolution and coarse range resolution. We assume that the extraneous peaks of the ambiguity function occur in a region of space and velocity where no targets are present.

In our simulations, we choose the duration of each pulse to be $T_p = 10 \times 10^{-6}$ s, the pulse period to be $T_R = 10^{-4}$ s, and take $N = 50$ pulses in the pulse train so that the duration of the entire pulse train is $T = NT_R = 5 \times 10^{-3}$ s. The bandwidth B of the pulse train is chosen to be $B = 3 \times 10^6$Hz. We take the center frequency to be 30GHz, which corresponds to a wavelength of $\lambda = 0.01$m.

The ambiguity function of this pulse train has the following properties.

- The Doppler resolution is $1/T = 200$ s^{-1}, which in the ordinary monostatic case would correspond to down-range velocity resolution of $\Delta V = \lambda/(2T) = 1$ m/s.
- The first ambiguous Doppler value is $1/T_R = 10^4$ s^{-1}, which would correspond to a monostatic velocity ambiguity of $\Delta V_{\max} = \lambda/(2T_R) = 50$ m/s.
- The delay resolution is $1/B \approx .3 \times 10^{-6}$ s, which would correspond to a monostatic range resolution of $\Delta r = c/(2B) = 50$ m.
- The first ambiguous delay is $T_R = 10^{-4}$ s, which corresponds to an ambiguous (monostatic) range of $\Delta r_{\max} = cT_R/2 = 1.5 \times 10^4$ m. This would be the maximum measurable unique range.

2) Area of Interest: The area of interest is a circular region with radius of 1000 m; points within this region differ by no more than 2000m, which is well within the unambiguous range of 15000 m. We assume that there are no scatterers outside the region of interest. The location of every point in the region is denoted by the vector $\boldsymbol{p} = r(\cos\theta, \sin\theta)$. The directions θ are sampled at intervals of $\pi/4$, while the lengths r are sampled at intervals of 25 m.

3) Velocities of Interest: The velocities are written $\boldsymbol{u} = s(\cos\phi, \sin\phi)$. We consider velocity magnitudes in the interval $[0, 30]$ m/s. The magnitudes s are sampled at intervals of 0.5 m/sec and the directions ϕ are sampled at intervals of $\pi/4$.

B. Examples

1) Single transmitter, two receivers: The point-spread function for a single transmitter and two receivers is shown in Figure 3. Here the transmitter is located at $\boldsymbol{y} = (0, -10000)$ m, the receivers are located at $\boldsymbol{z}_1 = (10000, 0)$ m and $\boldsymbol{z}_2 = (-10000, 0)$ m, the scene of interest is a disk centered at the origin with radius 1000 m, the target location is $225(\cos 45°, \sin 45°)$ m and the target velocity is $20(\cos 0, \sin 0)$ m/s.

We see that for this geometry, the point-spread function is indeed ridge-like.

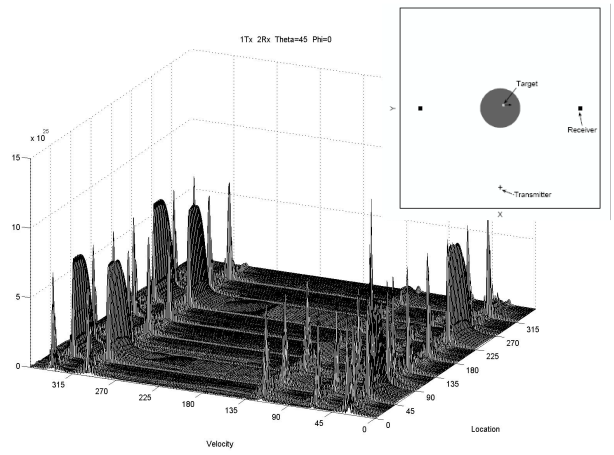

Fig. 3. This shows the geometry (not to scale) for one transmitter and two receivers, together with the the combined point-spread function.

2) Circular geometry: Figure 4 shows the point-spread function for a circular arrangement of 8 transmitters and 10 receivers. The transmitters are equally spaced around a circle of radius 10000 m; the receivers are equally spaced around a circle of radius 9000 m. The scene of interest has radius 1000 m. The true target location is $225(\cos 180°, \sin 180°)$ m and the true velocity is $20(\cos 180°, \sin 180°)$ m/s. For this geometry, there appear to be no ambiguities.

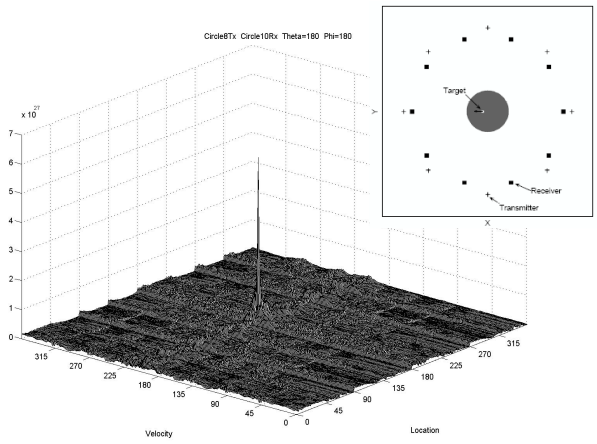

Fig. 4. This shows the geometry (not to scale) for 8 transmitters and 10 receivers arranged in a circle and the corresponding combined point-spread function.

3) Linear array: Figure 5 shows the point-spread function for a linear array of 11 transmitters and a single receiver. In this case, the transmitters are equally spaced along the line $-5000\text{m} \le x \le 5000\text{m}, y = 10000\text{m}$; the receiver is located at $(0, 10000)\text{m}$; the true target location is $225(\cos 135°, \sin 135°)$ m and the target velocity is $20(\cos 45°, \sin 45°)$ m/s.

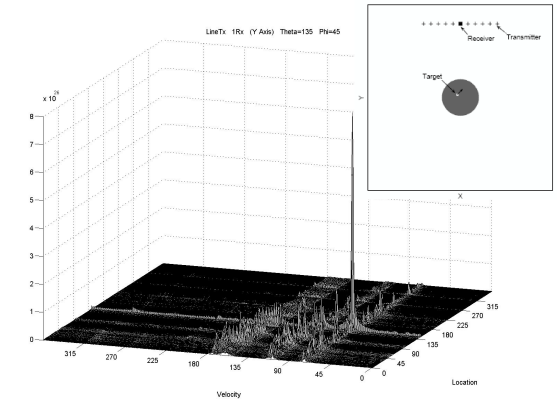

Fig. 5. This shows the geometry (not to scale) for a linear array 11 transmitters and a single receiver and the corresponding combined point-spread function.

VI. Reduction to Special Cases

A. Range-Doppler Imaging

We specialize to the case of range-doppler imaging by using a single transmitter and coincident receiver; in this case the point-spread function reduces to the classical radar ambiguity function [4], [8].

B. High-Range-Resolution Imaging

We recover SAR and ISAR by using high range-resolution (HRR) pulses, for which the ambiguity function is a narrow ridge extending along the ν axis. In these cases, we write

$$A_{\boldsymbol{y}}(\nu, \tau) = \overline{A}_{\boldsymbol{y}}(\tau), \tag{19}$$

with $\overline{A}_{\boldsymbol{y}}(\tau)$ sharply peaked around $\tau = 0$. This ambiguity function together with appropriate relative motion between sensor and target reduces to SAR and ISAR.

C. Diffraction Tomography

Diffraction tomography, which is also called *ultra-narrowband imaging*, uses a single frequency waveform $s(t) = \exp(-i\omega_0 t)$ (with $\tilde{s} = 1$) to interrogate a stationary object. In this case the data is

$$\psi^{\infty}_{\omega_0}(t, \boldsymbol{z}, \boldsymbol{y}) \approx \frac{e^{-ik_0 t}}{(4\pi)^2 |\boldsymbol{z}||\boldsymbol{y}|} F_{\infty}(\hat{\boldsymbol{y}}, \hat{\boldsymbol{z}})\,, \tag{20}$$

where the (Born-approximated) *far-field pattern* or *scattering amplitude* is

$$F_{\infty}(\hat{\boldsymbol{y}}, \hat{\boldsymbol{z}}) = \int e^{-ik_0(\hat{\boldsymbol{z}}+\hat{\boldsymbol{y}})\cdot\boldsymbol{x}} q(\boldsymbol{x})\, d^3x\,. \tag{21}$$

and where $k_0 = \omega_0/c$. We note that our incident-wave direction convention (from target to transmitter) is the opposite of that used in the classical scattering theory literature (which uses transmitter to target).

Our inversion formula is (10), where there is no integration over t. The resulting formula is

$$I_{k_0}(\boldsymbol{p}) = \int e^{ik_0(\hat{\boldsymbol{z}}+\hat{\boldsymbol{y}})\cdot\boldsymbol{p}}\, Q_{k_0}(\hat{\boldsymbol{z}}, \hat{\boldsymbol{y}}) F_{\infty}(\hat{\boldsymbol{y}}, \hat{\boldsymbol{z}})\, d\hat{\boldsymbol{y}}\, d\hat{\boldsymbol{z}} \tag{22}$$

where Q_{k_0} is the filter [5], [6]

$$Q_{k_0} = \frac{k_0^3}{(2\pi)^4} |\hat{\boldsymbol{y}} + \hat{\boldsymbol{z}}|. \tag{23}$$

which is closely related to the Jacobian J above. Here the factor of k_0^3 corresponds to three-dimensional imaging.

The associated point-spread function is

$$I_{k_0}(\boldsymbol{p}) \quad = \int \chi_{2k}(\boldsymbol{\xi}) e^{i\boldsymbol{\xi}\cdot(\boldsymbol{p}-\boldsymbol{x})}\, d^3\xi\; q(\boldsymbol{x})\, d^3x \tag{24}$$

where χ_{2k} denotes the function that is one inside the ball of radius $2k$ and zero outside.

D. Moving Target Tomography.

Moving Target Tomography [7] models the signal using a simplified version of (5). For this simplified model, our imaging formula (10) reduces to matched-filter processing [7] with a different filter for each location $\boldsymbol{p}$ and for each possible velocity $\boldsymbol{u}$.

VII. Conclusion

We see from (14) that the point-spread function for phase-space imaging is a weighted coherent sum of bistatic radar ambiguity functions.

It remains to analyze this point-spread function and determine whether ambiguities are present in phase-space imaging.

ACKNOWLEDGMENT

This work was supported by the Office of Naval Research, by the Air Force Office of Scientific Research[1] under agreement number FA9550-06-1-0017, by Rensselaer Polytechnic Institute, and by the National Research Council.

REFERENCES

[1] N. Bleistein, J.K. Cohen, and J.W. Stockwell, *The Mathematics of Multidimensional Seismic Inversion,* New York: Springer, 2000)

[2] B. Borden and M. Cheney, "Synthetic-Aperture Imaging from High-Doppler-Resolution Measurements," *Inverse Problems,* **21**, pp. 1–11 (2005).

[3] M. Cheney and B. Borden, "Imaging Moving Targets from Scattered Waves," *Inverse Problems* 24 (2008) 035005.

[4] C.E. Cook and M. Bernfeld, *Radar Signals,* New York: Academic Press, 1967.

[5] A.J. Devaney, "Inversion formula for inverse scattering within the Born approximation," Optics Letters, **7**, pp. 111–112 (1982).

[6] A.J. Devaney, "A filtered backpropagation algorithm for diffraction tomography", Ultrasonic Imaging, **4**, pp. 336–350 (1982).

[7] B. Himed, H. Bascom, J. Clancy, and M.C. Wicks, "Tomography of Moving Targets (TMT)", in *Sensors, Systems, and Next-Generation Satellites V.*, ed. H. Fujisada, J.B. Lurie, and K. Weber, Proc. SPIE Vol. 4540 (2001) pp. 608 – 619.

[8] N. Levanon, *Radar Principles,* New York: Wiley, 1988.

[9] C.J. Nolan and M. Cheney, "Synthetic Aperture Inversion," Inverse Problems, **18**, pp. 221–36 (2002)

[10] N.J. Willis, *Bistatic Radar*, Norwood, MA: Artech House, 1991.

[11] N.J. Willis and H.D. Griffiths, *Advances in Bistatic Radar*, Raleigh, North Carolina: SciTech Publishing, 2007.

[12] N.J. Willis, "Bistatic Radar," in *Radar Handbook*, M. Skolnik, ed., New York: McGraw-Hill, 1990.

[13] B. Yazici, M. Cheney, and C.E. Yarman, "Synthetic-aperture inversion in the presence of noise and clutter", Inverse Problems **22**, pp. 1705-1729 (2006) .